Atmospheric Environment 222 (2020) 117121

Contents lists available at ScienceDirect

Atmospheric Environment

journal homepage: http://www.elsevier.com/locate/atmosenv

Retrieval of surface $PM_{2.5}$ mass concentrations over North China using visibility measurements and GEOS-Chem simulations

Sixuan Li [a,b], Lulu Chen [c], Gang Huang [a,b,d,*], Jintai Lin [c,**], Yingying Yan [c], Ruijing Ni [c], Yanfeng Huo [e], Jingxu Wang [c], Mengyao Liu [c], Hongjian Weng [c], Yonghong Wang [f], Zifa Wang [b,g]

[a] State Key Laboratory of Numerical Modeling for Atmospheric Sciences and Geophysical Fluid Dynamics (LASG), Institute of Atmospheric Physics, Chinese Academy of Sciences, Beijing, 100029, China
[b] University of Chinese Academy of Sciences, Beijing, 100000, China
[c] Laboratory for Climate and Ocean-Atmosphere Studies, Department of Atmospheric and Oceanic Sciences, School of Physics, Peking University, Beijing, 100871, China
[d] Laboratory for Regional Oceanography and Numerical Modeling, Qingdao National Laboratory for Marine Science and Technology, Qingdao, 266237, China
[e] Anhui Institute of Meteorological Sciences, Hefei, 230031, China
[f] Institute for Atmospheric and Earth System Research / Physics, Faculty of Science, P.O. Box 64, 00014, University of Helsinki, Helsinki, Finland
[g] State Key Laboratory of Atmospheric Boundary Layer Physics and Atmospheric Chemistry, Institute of Atmospheric Physics, Chinese Academy of Sciences, Beijing, 100000, China

HIGHLIGHTS

- We integrate visibility data and GEOS-Chem simulations to estimate $PM_{2.5}$ concentrations in 2014 over North China.
- Visibility converted $PM_{2.5}$ are spatiotemporally consistent with $PM_{2.5}$ measurements.
- Our method provides a novel, plausible way to retrieve long-term variation of $PM_{2.5}$.

ARTICLE INFO

Keywords:
Visibility
Chemical transport model (CTM)
$PM_{2.5}$
Spatial pattern
Time series
North China plain (NCP)

ABSTRACT

Despite much effort made in studying human health associated with fine particulate matter ($PM_{2.5}$), our knowledge about $PM_{2.5}$ and human health from a long-term perspective is still limited by inadequately long data. Here, we presented a novel method to retrieve surface $PM_{2.5}$ mass concentrations using surface visibility measurements and GEOS-Chem model simulations. First, we used visibility measurements and the ratio of $PM_{2.5}$ and aerosol extinction coefficient (AEC) in GEOS-Chem to calculate visibility-inferred $PM_{2.5}$ at individual stations (SC-$PM_{2.5}$). Then we merged SC-$PM_{2.5}$ with the spatial pattern of GEOS-Chem modeled $PM_{2.5}$ to obtain a gridded $PM_{2.5}$ dataset (GC-$PM_{2.5}$). We validated the GC-$PM_{2.5}$ data over the North China Plain on a 0.3125° longitude x 0.25° latitude grid in January, April, July and October 2014, using ground-based $PM_{2.5}$ measurements. The spatial patterns of temporally averaged $PM_{2.5}$ mass concentrations are consistent between GC-$PM_{2.5}$ and measured data with a correlation coefficient of 0.79 and a linear regression slope of 0.8. The spatial average GC-$PM_{2.5}$ data reproduce the day-to-day variation of observed $PM_{2.5}$ concentrations with a correlation coefficient of 0.96 and a slope of 1.0. The mean bias is less than 12 $\mu g/m^3$ (<14%). Future research will validate the proposed method using multi-year data, for purpose of studying long-term $PM_{2.5}$ variations and their health impacts since 1980.

1. Introduction

Particulate matter with diameter less than 2.5 μm ($PM_{2.5}$) affects the climate, visibility and human health (Lelieveld et al., 2015; Allen et al., 2014; Wang et al., 2015). According to a Global Burden of Disease study (Lim et al., 2012), global $PM_{2.5}$ pollution accounted for 3.1 million

* Corresponding author. State Key Laboratory of Numerical Modeling for Atmospheric Sciences and Geophysical Fluid Dynamics (LASG), Institute of Atmospheric Physics, Chinese Academy of Sciences, Beijing, 100029, China.
** Corresponding author.
E-mail addresses: hg@mail.iap.ac.cn (G. Huang), linjt@pku.edu.cn (J. Lin).

https://doi.org/10.1016/j.atmosenv.2019.117121
Received 1 February 2019; Received in revised form 4 November 2019; Accepted 6 November 2019
Available online 9 November 2019

deaths in 2010, predominantly in China and India. A recent study revealed that transboundary $PM_{2.5}$ pollution associated with international trade and atmospheric transport together caused 0.76 million premature deaths worldwide in 2007 (Zhang et al., 2017). Studies on fine particle matter health impacts and climate influences require historical $PM_{2.5}$ data. Therefore, to fully assess the health impacts of $PM_{2.5}$, it is crucial to get access to long-term $PM_{2.5}$ data across multiple decades. However, to our knowledge, long-term $PM_{2.5}$ data are lacking especially in developing countries.

Surface $PM_{2.5}$ mass concentrations in China are measured typically by either Tapered Element Oscillating Microbalances (TEOM) or BETA-ray instruments. In China, continuous $PM_{2.5}$ measurements are sparse before 2013. The Chinese official air quality monitoring network measures $PM_{2.5}$ and other pollutants since 2013, mostly in the urban areas. These data form the basis for many recent studies on the spatial and temporal characteristics of urban air pollution and their causes over China (Liu et al., 2018; Wang et al., 2014; Ge et al., 2018). However, these measurement data cannot be used to analyze long-term trends and variability of $PM_{2.5}$ and resulting health effects. Therefore, alternative approaches to retrieving surface $PM_{2.5}$ concentrations were developed in the past decades.

Aerosol Optical Depth (AOD) data based on modern satellite remote sensing have been used widely to retrieve surface $PM_{2.5}$ concentrations due to their good spatial coverage. AOD data are available from multiple satellite instruments, such as the Moderate Resolution Imaging Spectroradiometer (MODIS, since 2000), the Multiangle Imaging SpectroRadiometer (MISR, since 2000), and the Sea-viewing Wide Field-of-view Sensor (SeaWiFS, since 1998) (Liu et al., 2017a). These AOD data have been combined with chemical transport model simulations or statistical approaches to derive surface $PM_{2.5}$ (Boys et al., 2014; Geng et al., 2015; van Donkelaar et al., 2010, 2015).

van Donkelaar et al. (2010) estimated the global distribution of $PM_{2.5}$ using satellite MODIS and MISR AOD products and GEOS-Chem simulations from 2001 to 2006. Their estimated $PM_{2.5}$ values show good agreement with observed $PM_{2.5}$ over North America. Using the same method and MODIS, MISR and SeaWiFS AOD data, Boys et al. (2014) produced a 15-year time series (1998–2012) of surface $PM_{2.5}$ concentrations worldwide, which agreed well with the situ measurements in Eastern U.S. van Donkelaar et al. (2015) used the Geographically Weighted Regression (GWR) statistical model to improve the $PM_{2.5}$ inference from AOD and GEOS-Chem simulations. Their analysis showed that local variability in surface elevation and urban emissions are important sources of uncertainty in retrieving $PM_{2.5}$ concentrations. Using satellite AOD data and high-resolution GEOS-Chem simulations, Geng et al. (2015) estimated surface $PM_{2.5}$ concentrations over China during 2006–2012, after using CALIOP aerosol vertical profile data to correct for model biases. They found very good spatial agreement between satellite-derived and measured $PM_{2.5}$ concentrations.

However, there are a number of limitations embedded in such satellite-based $PM_{2.5}$ inference approaches. Model simulations are subject to errors in the model representations of atmospheric processes, especially the vertical mixing and transport that directly affect the simulated aerosol vertical profiles (Lin and McElroy, 2010; Liu et al., 2018). Satellite-based AOD datasets are subject to a large number of missing values due to screening for cloudy and strongly surface reflecting scenes. The AOD datasets may have a low sampling bias, because high aerosol scenes may be mis-treated as cloudy ones and screened out (Lin and Li, 2016). In addition, there are no reliable satellite AOD data over land before 1998.

Satellite AOD data can also be combined with statistical models or machine learning approaches to infer surface $PM_{2.5}$ concentrations. Taking meteorology and land use information into model, Ma et al. (2014) estimated surface $PM_{2.5}$ concentrations using AOD from MODIS and MISR as a primary predictor. Zheng et al. (2016) constructed linear mixed-effects models to convert MODIS AOD data and other predictors to ground-level $PM_{2.5}$ concentrations over three major industrialized regions in China. They corrected the predicted $PM_{2.5}$ concentrations by observed $PM_{2.5}$. Li et al. (2017) applied a Geo-Intelligent Deep Learning approach to estimate $PM_{2.5}$ over China, and they showed that in 2015 over 80% of Chinese lived in areas with annual mean $PM_{2.5}$ concentrations above the WHO IT-1 standard levels (35 $\mu g/m^3$). Nonetheless, these statistical or machine learning approaches may have difficulties in establishing/explaining the causality between $PM_{2.5}$ and predictors, which poses the question of how the established relationships can be extrapolated to other times and/or regions. The coefficient of determination (R^2) of such methods declines substantially from 0.41 to 0.98 when the training dataset is used to 0.31–0.55 when the predictive dataset is used (Wei et al., 2019). In addition, satellite AOD data have their own limitations, as mentioned above.

Visibility measurements available for multiple decades from ground meteorological stations have also been used, together with statistical models, for $PM_{2.5}$ inference. Visibility represents horizontal light extinction, which is highly related with the amount of $PM_{2.5}$, its chemical compositions, size distributions, optical properties, and hygroscopicity (Charlson, 1969; Sinclair et al., 1974; Song et al., 2003). Visibility and $PM_{2.5}$ concentrations are negatively correlated with a power law relationship (Zhao et al., 2011; Zhang et al., 2019). Based on visibility data from 674 meteorological monitoring sites and a statistical model, Liu et al., 2017a inferred the long-term (1957–1964 and 1973–2014) changes of $PM_{2.5}$ pollution in China. They found $PM_{2.5}$ concentrations reached 60–80 $\mu g/m^3$ over the northern part of the North China Plain during the 1950s–1960s, increasing to levels generally higher than 90 $\mu g/m^3$ since then. Shen et al. (2016) retrieved historical (1979–2003) $PM_{2.5}$ mass concentrations in Xi'an using visibility measurements and an exponential regression model, and they found decreasing trends by -4.6 $\mu g/m^3$/year and -12.1 $\mu g/m^3$/year during 1979–1996 and 2007–2011, respectively, in contrast to a growth during 1997–2007 by 8.8 $\mu g/m^3$/year. However, statistical models are subject to abovementioned limitations.

This study presents a new method to retrieve surface $PM_{2.5}$ mass concentrations using GEOS-Chem simulations and surface visibility measurements. The method is inspired by our present study (Lin and Li, 2016; Lin et al., 2014) that used GEOS-Chem and visibility data to infer AOD over East China, which showed high consistency with AErosol RObotic NETwork (AERONET) and MODIS AOD data in terms of a low bias and high temporal and spatial correlations. Here we proposed a similar method to retrieve $PM_{2.5}$ concentrations over the NCP in January, April, July and October 2014 (i.e., covering four seasons). In particular, we used GEOS-Chem to help convert visibility to $PM_{2.5}$ concentration at each site and then to a gridded space, in order to facilitate further applications such as health impact analysis. We further validated the retrieved $PM_{2.5}$ data against ground $PM_{2.5}$ measurements.

2. Data and methods

2.1. Surface $PM_{2.5}$ mass concentration measurements

Hourly surface $PM_{2.5}$ concentration measurements were obtained from the China National Environmental Monitoring Center (CNEMC). The filled circles in Fig. 1 show the 396 observation sites over the NCP used here. The sites are concentrated in urban areas and lack coverage in rural and remote areas. Thus the observed data may not fully represent the regional air quality.

At these 396 sites, $PM_{2.5}$ concentrations are measured by either TEOM or Beta-attenuation instruments. Quality control is done through a fully automatic outlier detection method for four types of outliers: temporal and spatial inconsistency, low variance, periodic calibration exceptions, and PM_{10} concentrations being lower than $PM_{2.5}$ concentrations (Wu et al., 2018). Additionally, we required that there are at least 20 hourly data for each day, 20 days per month, 2 months in January, April, July and October 2014. We chose the four months to represent individual seasons, instead of choosing all months, to reduce

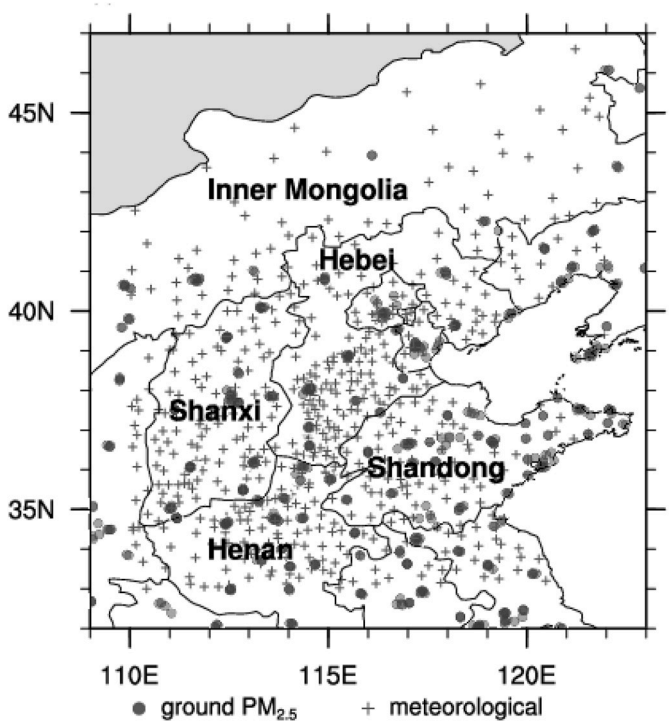

Fig. 1. Ground $PM_{2.5}$ observation sites (filled circles) and meteorological stations (gray crosses) over the NCP.

the computational costs of respective GEOS-Chem simulations. When comparing with $PM_{2.5}$ measurements, we excluded data at times when either visibility-converted $PM_{2.5}$ or measured $PM_{2.5}$ data were missing.

2.2. Visibility and other meteorological data

Visibility, temperature, wind speed and Relative Humidity (RH) measurements at 610 sites in January, April, July and October 2014 were obtained from Chinese Meteorological Administration (CMA). The gray crosses in Fig. 1 show the meteorological sites.

For our study period, visibility is measured automatically by Forward Scattering Visibility Meter (FSVM) which has a scattering angle of 30°–50°. The instrument ignores the absorption of light by the atmosphere, thus the derived scatter coefficient is scaled up by an embedded algorithm to account for absorption and better represent the total extinction coefficient before the value is converted to visibility (Tan et al., 2010). Chinese meteorological stations mostly use the HY-V35 automatic visibility instrument manufactured by Huayun Shengda Company, with core components of the instrument purchased from Vaisala, Finland. HY-V35 passed the assessment of various indicators of CMA on May 2011. The instrument measures forward scattering in the angle of 45°. In the instrument manual, it points out that $K = 3.0$ in the Koschmeider equation that connects light extinction and visibility.

This automatic measurement is different from the manual measurement before 2013, i.e., by human eyes. Manual observations tend to give larger visibility values than automatic measurements, whereas their linear trends are highly consistent (Fan et al., 2017; Liu et al., 2017b). Therefore, precaution should be taken when combining manual and automatic visibility measurements for long-term $PM_{2.5}$ studies, which is the focus of our future studies. For example, according to the Koschmeider equation, $AEC = K/V$, $K = -\ln\varepsilon$, and ε denotes visual contrast. According to the regulations of the International Meteorological Organization, $\varepsilon = 0.05$ ($K = 3.0$) for instrument measurement. When manual measurements of visibility are used for historical analyses in future research, we will change the value of K to 3.9 (Lin et al., 2104; Lin and Li, 2016). In addition, we will consider discontinuity issues about long-term visibility data such as site movement and reporting standard. Observations taken at night and under heavy cloudy conditions can also be uncertain. Therefore, a careful filtering and quality control process will be performed before these data are used to study long-term trend. Nevertheless, this study only focuses on the automatic visibility measurements.

The visibility observations are hourly data beginning at 00:00 UTC (08:00 Beijing Standard Time). Quality control for visibility data is shown in Section. 2.4. Other meteorological data are also available hourly. Note that compared to satellite AOD data, visibility data provide a much longer time series of information for $PM_{2.5}$ inference since the 1950s to help evaluate the long-term changes in $PM_{2.5}$ and related health impacts. Compared to $PM_{2.5}$ measurement sites, meteorological stations are spatially more homogeneous and are available at urban, rural and remote areas, providing better spatial representativeness.

2.3. GEOS-Chem model

We used the nested GEOS-Chem model for China (version 11–01, http://wiki.seas.harvard.edu/geos-chem/index.php/Main_Page) to simulate the ratio between surface $PM_{2.5}$ concentration and Aerosol Extinction Coefficient (AEC) for converting the visibility-derived near-surface AEC to $PM_{2.5}$. Driven by the GEOS-FP assimilation meteorology from the Goddard Earth Observing System (GEOS) of the NASA Global Modeling and Assimilation Office, the nested model has a horizontal resolution of 0.3125° longitude x 0.25° latitude with 47 vertical layers, and the lowest 10 layers are of ~130 m thickness each. The lateral boundary conditions of nested model are taken every 3 h from a global GEOS-Chem simulation at 2.5° longitude x 2° latitude. Spin-up time for nested model and global model are 15 days and one month, respectively. The scheme of planetary boundary layer employs a non-local scheme implemented by Lin and McElroy (2010). Model convection is simulated with the relaxed Arakawa–Schubert scheme (Rienecker et al., 2008).

Both the global and nested GEOS-Chem models are run with the NOx-Ox-hydrocarbon-aerosol-bromine tropospheric chemistry mechanism with online aerosols. Aerosols simulated include secondary inorganic aerosols (SIOA, including sulfate, nitrate and ammonium), secondary organic aerosols (SOA), primary organic aerosols (POA), black carbon (BC), dust and sea salt. The ammonium-sulfate-nitrate-water system is calculated by ISORROPIA II thermodynamic equilibrium model (Fountoukis and Nenes, 2007), with updates on heterogeneous sulfate and nitrate processes (Zhang et al., 2015). Natural dust particles are emitted with the DEAD scheme (Fairlie et al., 2010; Zhang et al., 2013). The calculation of SOA species are parameterized by Pye and Seinfeld (2010). The parameterization of sea salt is from Jaegle et al. (2011). Uptake of the hydroperoxyl radical on aerosols and representation of anthropogenic aromatics follow Lin et al. (2012) and Ni et al. (2018).

Monthly gridded anthropogenic emissions in China are taken from the Multi-resolution Emission Inventory for China (MEIC, www.meicmodel.org; Geng et al., 2017) for 2014 for nitrogen oxides (NOx), carbon monoxide (CO), sulfur dioxide (SO_2), BC and POA. Following Zhang et al. (2015), emissions of anthropogenic fine dust are also included, by taking primary $PM_{2.5}$ emissions from MEIC. For non-methane volatile organic compounds (NMVOC) emissions, the spatial pattern, seasonal pattern and ratios of individual compounds to the total NMVOC are fixed, with the total amount of NMVOC scaled to each specific study year according to the national total amount of NMVOC in MEIC in 2014. Biomass burning emissions are taken from the monthly GFED4 datasets (Giglio et al., 2013). Biogenic emissions of NMVOC follow MEGANv2.1 (Guenther et al., 2012). Soil emissions of NOx employ the parameterization from Hudman et al. (2012).

Future research aiming to combine model simulations with visibility data for historical $PM_{2.5}$ studies could use the MERRA2 assimilated meteorological data available since 1980 and the monthly emission data from the Community Emissions Data System available since 1750. A

historical analysis, however, is out of the scope of this study.

2.4. Retrieval method

As shown in Fig. 2, our retrieval method contains multiple steps. First, we conducted quality control for visibility data, following previous studies (Husar et al., 2000; Lin et al., 2014; Li et al., 2016). Fine particle matter and relative humidity is the two main factors affecting visibility. Observational results (Chen et al., 2012) show that when RH < 90%, low visibility is largely influenced by aerosol volume concentration; while for RH > 90%, indicative of the formation of fogs and precipitation, the increase of RH is dominantly responsible for the decrease of visibility. Therefore, to reduce the effect of non-aerosol factors on visibility, we excluded visibility records when RH exceeded 90%. This choice is consistent with previous studies (Craig and Faulkenberry, 1979; Zhao et al., 2011). We further excluded data that may be affected by blown snow from the ground, i.e., when air temperature is below −29 °C and wind speed above 16 km/h. If the maximum value of visibility data at a site in the clean area (median visibility > 11 km) within a month is smaller than 12 km, all data at that site in that month were excluded; this situation indicates erroneous data record. To remove potentially erroneous data spikes, if the daily mean visibility on a day is lower than one third of the value both on the day before and on the day after, data on that day were excluded (Husar et al., 2000).

Second, we converted the quality controlled visibility data to hourly near-surface AEC. According to the Koschmieder Equation, near-surface AEC at 550 nm is inversely proportional to visibility if the effect of air molecules is neglected: AEC = K/V. This formula is often used for the conversion between visibility and aerosol extinction coefficient (Husar et al., 2000; Lin et al., 2014; Xu et al., 2005). Here V represents the observed visibility, and K = -lnε is the Koschmieder constant. For FSVM, the contrast threshold ε is chosen as 5%, with K equal to 3.0 (Li and Sun, 2009; Zeng and Wang, 1999). In order to reduce the optical influence of air molecules and correct for other potential errors at clean (high visibility) situations, we used a modified formula to relate visibility and AEC: AEC = K/V–K/V_0, where V_0 = 70 km (Lin et al., 2014).

Third, we adopted the hourly ratio of $PM_{2.5}$ to AEC simulated by GEOS-Chem to scale the visibility converted AEC to obtain the visibility-inferred $PM_{2.5}$ concentrations at individual sites (hereafter referred to as Station Concerted-$PM_{2.5}$):

$$(PM_{2.5})_{SC} = AEC \times \frac{(PM_{2.5})_{\text{model}}}{AEC_{\text{model}}}$$

For a particular site, the modeled ratio of $PM_{2.5}$ to AEC was taken as the value interpolated from nearby model grid cells through bilinear interpolation, with the time of model results matching that of the hourly visibility data. At each model grid cell, the model $PM_{2.5}$ concentration was summed over the concentrations of fine dust (DST1 + 0.38 × DST2 in the model), fine sea salt particles (SALA in the model), BC, POA (assumed to be 1.8 times the mass of primary organic carbon), and SIOA. The model AEC was calculated based on the optical effects of these $PM_{2.5}$ components and additional coarse mode dusts (DST3 and DST4) and coarse sea salt particles (SALC), with their hygroscopicity accounted for (Lin et al., 2016) using the observed RH at respective meteorological station. Inclusion of coarse particles in calculating model AEC ensures the consistency with visibility-inferred AEC that is affected by both fine and coarse particles. Considering that the measured $PM_{2.5}$ and visibility data are near-surface, we choose the values of model $PM_{2.5}$ and AEC in the bottom model layer (i.e., from the ground to approximately 130 m). Then, we obtained a Station-Converted hourly $PM_{2.5}$ dataset in January, April, July and October 2014 over the NCP. The daily mean $PM_{2.5}$ data were averaged from the hourly data.

Fourth, we converted the station-specific daily mean $PM_{2.5}$ data to gridded data at a horizontal resolution of 0.3125° longitude x 0.25°

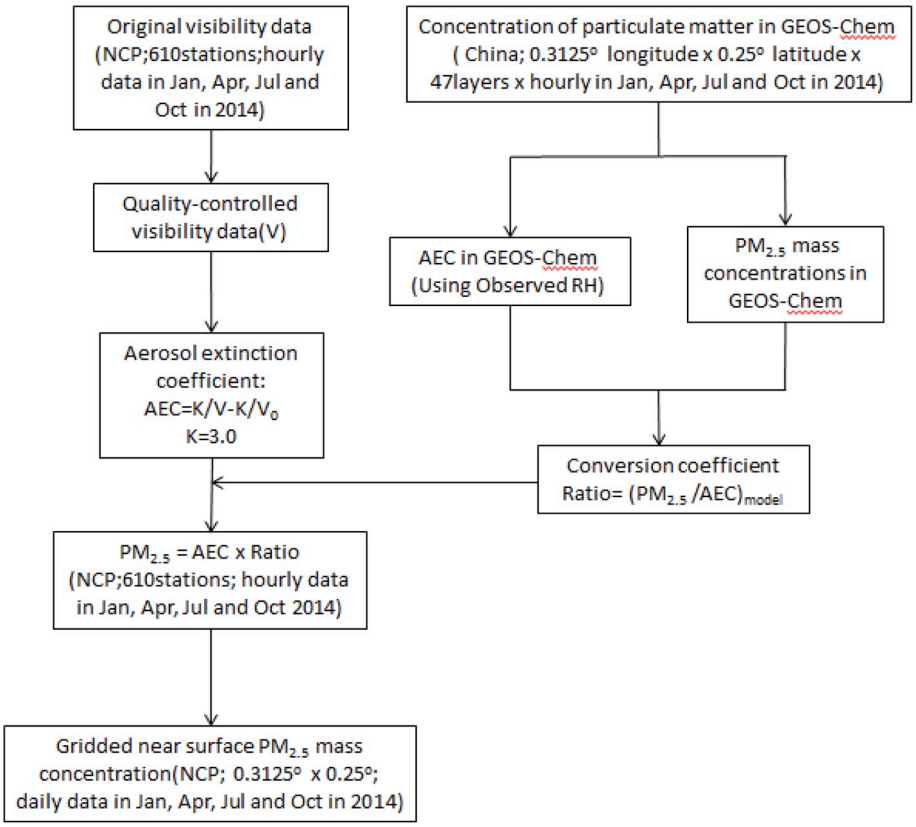

Fig. 2. A flowchart for retrieval of gridded $PM_{2.5}$ mass concentration data using visibility measurements and GEOS-Chem simulations. Data sources are shown in parentheses.

latitude, according to the resolution of GEOS-Chem. The resulting dataset is referred to as Grid-Converted $PM_{2.5}$. There are two purposes for this station-to-grid conversion. The station-based data lack continuous spatial coverage needed for health impacts studies. Also, the station-based visibility measurements are subject to instrument errors and representation errors, i.e., the measured values may be affected by local pollution sources and other factors and thus not fully representative of the actual pollution level in the surrounding area. In fact, visibility data may contain certain "noise" spatially, as shown in Lin et al. (2014) and in Sect. 3.3.

We tested 8 candidate methods for this station-to-grid conversion, and finally selected a method, Case 7, that has the best performance; see below for evaluation statistics and Sect. 3.2 for the selection process. All cases but Case 2 and Case 3 involved matching a grid cell center to surrounding visibility stations within a certain radius. We tested radii of 0.1°, 0.2°, 0.3°, 0.4°, 0.5°, 0.6°, 0.7°, 0.8°, 0.9°, 1.0°, 1.5° and 2°. The larger the radius is, the higher extent the Station-Converted $PM_{2.5}$ data are spatially smoothed.

$$\text{Case1}: c^{F}_{d,i} = median(c^{SC}_{d,i})$$

$$\text{Case2}: c^{F}_{d,i} = c^{Cres}_{d,i}$$

$$\text{Case3}: c^{F}_{d,i} = \sum_{i=1}^{n}\left(\frac{r_i^{-1}}{\sum_{i=1}^{n} r_i^{-1}}\right)\cdot c^{SC}_{d,i}$$

$$\text{Case4}: c^{F}_{d,i} = median\left(\frac{c^{SC}_{d,i}}{c^{M}_{d,i}}\right)\cdot c^{M}_{d,i}$$

$$\text{Case5}: c^{F}_{d,i} = \frac{median(c^{SC}_{m,i})}{c^{M}_{m,i}}\cdot c^{M}_{d,i}$$

$$\text{Case6}: c^{F}_{d,i} = \frac{c^{M}_{m,i}}{median(c^{SC}_{m,i})}\cdot median(c^{SC}_{d,i})$$

$$\text{Case7}: c^{F}_{d,i} = \frac{c^{M}_{m,i}\Big/ mean(c^{M}_{m,i})}{c^{SC}_{m,i}\Big/ mean(c^{SC}_{m,i})}\cdot median(c^{SC}_{d,i})$$

$$\text{Case8}: c^{F}_{d,i} = \frac{c^{M}_{m,i}\Big/ mean(c^{M}_{m,i})}{c^{Cres}_{m,i}\Big/ mean(c^{Cres}_{m,i})}\cdot c^{Cres}_{d,i}$$

In these eight candidate methods to convert station-specific to gridded $PM_{2.5}$ data, $c^{F}_{d,i}$ denotes the finally obtained daily mean $PM_{2.5}$ concentration on day d at grid cell i. The superscript F denotes final, M denotes model, SC denotes Station Converted, and Cres denotes Cressman interpolation. The subscript r denotes distance, d denotes day, m denotes month, i denotes grid cell i, and i' denotes the grid cell in which the visibility measurement station is located. The function "mean" denotes the average over all grid cells, and "median" denotes the median value among the selected grid cells.

Of these 8 methods, Cases 1–3 utilized the Station-Converted $PM_{2.5}$ data alone without further using GEOS-Chem simulations. Case 1 assigned to a grid cell the median value from stations within a certain radius of the grid cell center. Cases 2 and 3 used the Cressman and the Inverse Distance Weight (IDW) interpolation methods, respectively.

Cases 4–8 used the spatial variability simulated by GEOS-Chem to facilitate the station-to-grid conversion. As shown in Sect. 3.1, the GEOS-Chem simulated spatial distribution of $PM_{2.5}$ outperforms the distribution of visibility-converted station-based data. In Case 4, for a given grid cell "i" on each day, we found all stations within a certain radius of the grid cell center, calculated the ratios of Station-Converted $PM_{2.5}$ to Modeled $PM_{2.5}$ (at the grid cells in which these visibility stations are located), and then used the median value of these ratios to scale the Modeled $PM_{2.5}$ at grid cell "i". Case 5, aiming to eliminate the noise in the day-to-day variability, was similar to Case 4 except that the ratios were based on monthly (rather than daily) mean $PM_{2.5}$ data. Here, to reduce the monthly average calculation errors caused by missing values, we chose the median value of all stations within a certain radius of the grid cell center to match the model $PM_{2.5}$, and then used data on the days when Station-Converted $PM_{2.5}$ and model $PM_{2.5}$ are both available. Case 6 was similar to Case 5, except that the scaling was based on the (spatial) median of Station-Converted $PM_{2.5}$ data.

Cases 7 and Case 8 were designed based on the fact that Modeled $PM_{2.5}$ data were spatially consistent with $PM_{2.5}$ measurements and had a lower mean bias (see Sect. 3.1). The two cases used the spatial pattern (shape) of model $PM_{2.5}$ data to facilitate the station-to-grid conversion. For Case 7, we first calculated the monthly Modeled $PM_{2.5}$ at each grid cell normalized to its spatial average, calculated the respective value for Station-Converted $PM_{2.5}$., and then derived their ratio. The calculation of monthly mean values and the sampling of available grid cells were the same as in Case 5. We then used this ratio to scale the result derived from Case 1 to finally obtain the gridded and spatial shape-adjusted daily $PM_{2.5}$ data. Case 8 was similar to Case 7, except that Station-Converted $PM_{2.5}$ data are replaced by Cressman-interpolated gridded data from Case 2.

Evaluation of the 8 station-to-grid conversion methods was based on how each method led to high spatial and temporal (i.e., day-to-day across the four months) consistencies with the actual $PM_{2.5}$ measurements. A few indicators were used to evaluate the consistency, including bias, correlation coefficient, slope of a linear regression, root mean square error (RMSE). We applied the Reduced Major Axis (RMA) regression, which is more appropriate than the Ordinary Least Square regression when independent variable x contains errors, to estimate the slope and intercept.

3. Spatio-temporal variability of measured, modeled, Station-Converted and Grid-Converted $PM_{2.5}$

3.1. Comparison of Station-Converted, modeled and measured $PM_{2.5}$

Fig. 3 compares the spatial distributions of (a) observed, (b) Station-Converted, (c) Station-Converted and sampled based on available observations, (d) modeled and (e) Grid-Converted $PM_{2.5}$ concentrations over the NCP averaged over January, April, July and October 2014. From the observed data (Fig. 3a), which represent urban air quality, high $PM_{2.5}$ pollution occur over southern Hebei. The highest $PM_{2.5}$ concentrations reach 170.4 μg/m^3, due to the combined effects of large emissions, efficient secondary formation and unfavorable conditions for pollution outflow. $PM_{2.5}$ concentrations are lower over the northern parts of Hebei and Shanxi, Shandong Peninsula and Inner Mongolia, due to lower emissions and favorable topographical and meteorological conditions for pollution removal/transport (Zheng et al., 2018; Zhang et al., 2018). The domain average $PM_{2.5}$ concentration is 83.8 μg/m^3.

Fig. 3b shows the Station-Converted $PM_{2.5}$ data, which are more much regionally representative than the $PM_{2.5}$ observations (Fig. 3a) and still capture the observed spatial pattern (from urban sites). Since the Station-Converted $PM_{2.5}$ data are not spatially collocated with $PM_{2.5}$ observations, we choose the median value of the converted $PM_{2.5}$ data from all stations within a 0.2° radius of each $PM_{2.5}$ observation station (Fig. 3c). Such re-sampled data reveal several locations where Station-Converted $PM_{2.5}$ overestimate the observed values significantly.

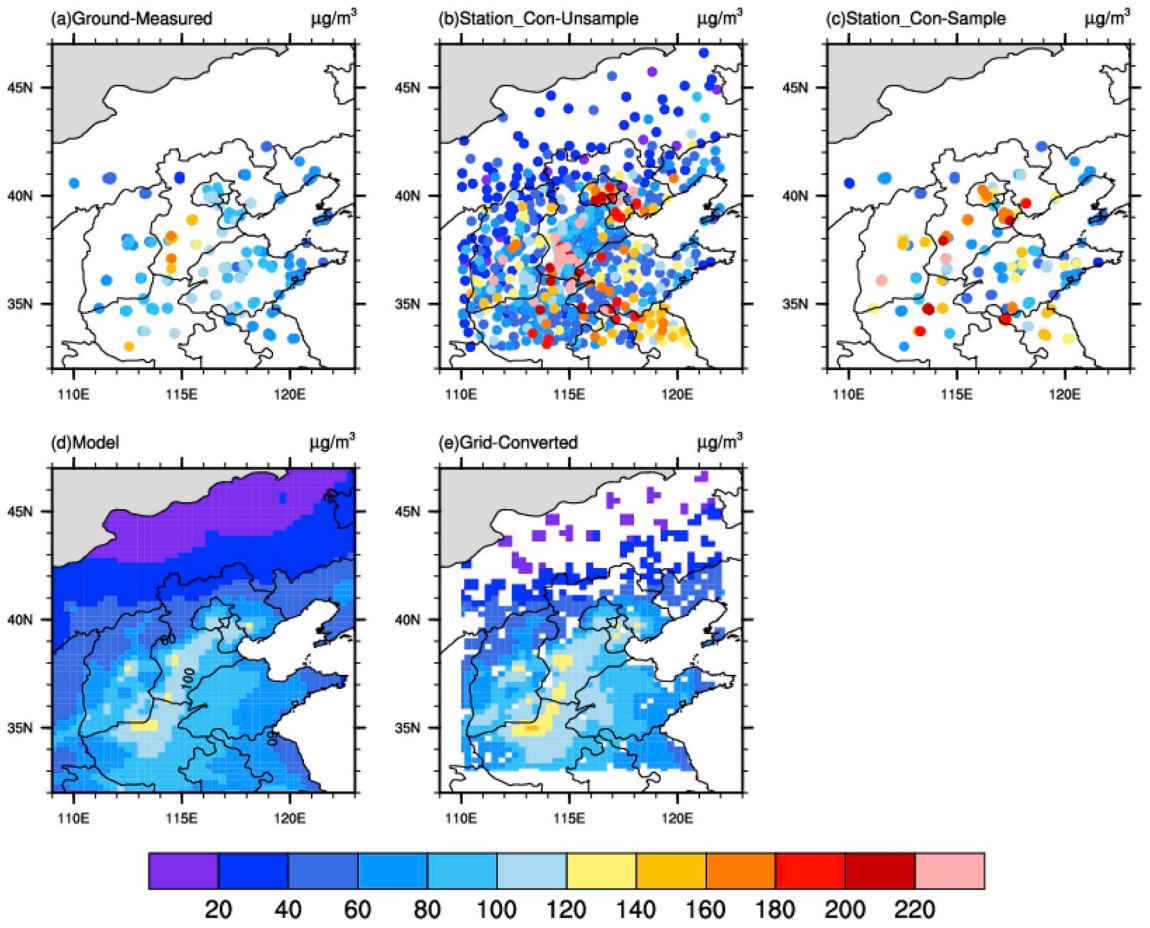

Fig. 3. Spatial distributions of (a) observed (ground $PM_{2.5}$ observation sites), (b) Station-Converted (based on visibility measurement sites), (c) Station-Converted and sampled with observation times and locations (ground $PM_{2.5}$ observation stations), (d) modeled (simulated by GEOS-Chem), and (e) Grid-Converted (visibility-converted for grid cells under Case 7, with a radius of 0.3°) $PM_{2.5}$ concentrations averaged over January, April, July and October 2014. The black lines show provincial borders.

Averaged over the NCP, the Station-Converted concentration is 109.8 μg/m^3, with an overestimate by 26.0 μg/m^3. The scatter plots in Fig. 4 also show significant positive biases of Station-Converted $PM_{2.5}$ data, especially when the pollutant concentrations are high.

GEOS-Chem captures the observed spatial distribution of $PM_{2.5}$ concentrations averaged over the four months in 2014 (Fig. 3d). As for model and Grid-Converted $PM_{2.5}$, we match the observation by choosing the grid cell in which the observation station is located. In particular, Fig. 4a shows that when sampled coincidently with the observations, the modeled $PM_{2.5}$ results have a small positive bias (by 2.5 μg/m^3). The

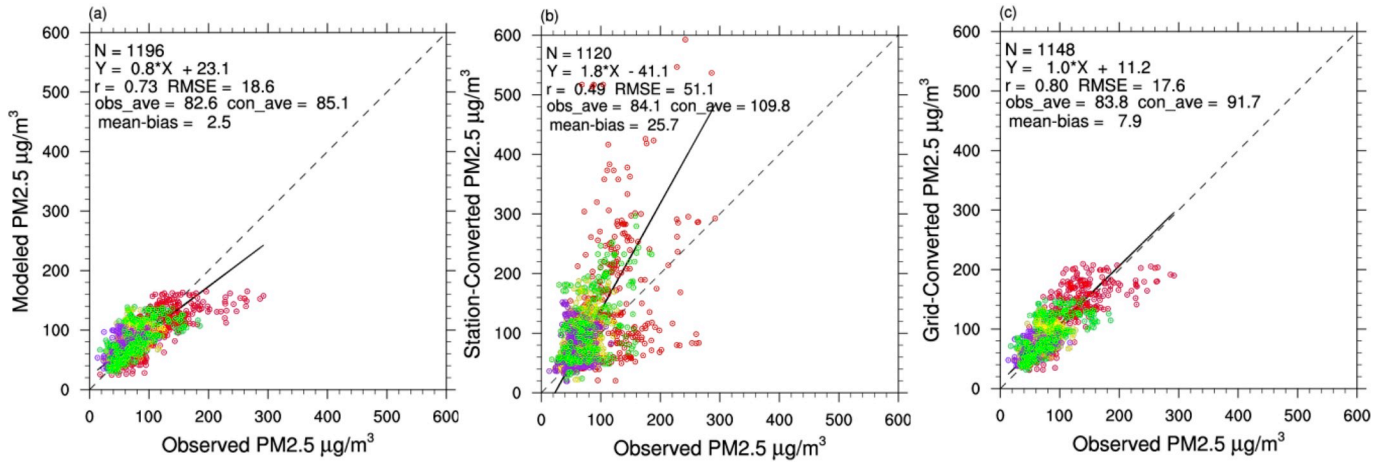

Fig. 4. Scatter plots of (a) modeled, (b) Station-Converted and (c) Grid-Converted (Case 7, with a radius of 0.3°) $PM_{2.5}$ (y-axis) with respect to $PM_{2.5}$ observations (x-axis). A data point in the figure represents the monthly mean values (red-January, yellow-April, purple-July, green-October) at a station. The dotted line depicts the 1:1 relationship, and the solid line depicts the RMA regression line. Statistical analysis results are shown in each panel. (For interpretation of the references to colour in this figure legend, the reader is referred to the Web version of this article.)

model has a high spatial correlation coefficient (0.73) with the observed data, much higher than the correlation coefficient for the Station-Converted data (0.49) (Fig. 4b). The modeled data also have significantly lower RMSE than the Station-Converted data (Fig. 4a and b). These results suggest that the model better captures the spatial distribution of $PM_{2.5}$ observations than the visibility-based data do.

Fig. 5 further evaluates the day-to-day variations of modeled and Station-Converted $PM_{2.5}$ concentrations against the observations in the four months. Modeled and Station-Converted data were sampled based on the observations; and results were averaged over the NCP on each day. Although both the modeled and Station-Converted $PM_{2.5}$ can capture the day-to-day variation of the observed data, the capability of Station-Converted data is better, especially with a higher correlation coefficient (0.96 versus 0.84). However, the modeled data is better than the Station-Converted ones in terms of mean bias and RMSE. Note that because of the difference in data averaging, the values for bias here are slightly different from those in the discussion of spatial distribution.

3.2. Evaluation of Grid-Converted $PM_{2.5}$ data derived from 8 candidate station-to-grid mapping methods

This section evaluates the Grid-Converted $PM_{2.5}$ data derived from 8 candidate station-to-grid mapping approaches presented in Sect. 2.4. Such mapping is based on the preference for health impact studies to having high spatial coverage and, for a few mapping approaches, an attempt to take advantage of the GEOS-Chem model capability in capturing the spatial pattern of $PM_{2.5}$ observations. As mentioned in Sect. 2.4, the evaluation focuses on whether the Grid-Converted data can

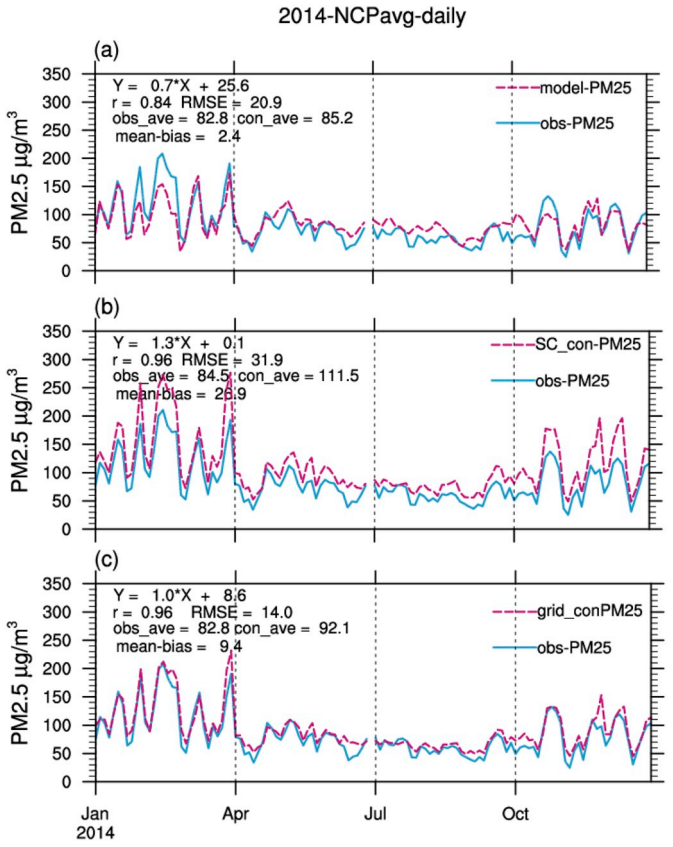

Fig. 5. Day-to-day variation of (a) modeled, (b) Station-Converted and (c) Grid-Converted (Case 7, with a radius of 0.3°) $PM_{2.5}$ with respect to $PM_{2.5}$ observations in January, April, July and October 2014. For each day, $PM_{2.5}$ concentrations are averaged over all stations in the NCP. Statistical analysis results are presented in each panel. Modeled, Station-Converted and Grid-Converted data are sampled based on the observations.

capture both the spatial and temporal (day-to-day) variations of observed $PM_{2.5}$.

Fig. 6 shows the evaluation statistics for each case, as a function of the distance (radius) from the visibility station to the grid cell center. As the mapping radius increases, the spatial feature of Grid-Converted $PM_{2.5}$ is further smoothed and the spatial details are further lost. For temporal (day-to-day) correlation evaluation (Fig. 6b), data on each day are averaged over all $PM_{2.5}$ measurement sites. In general, results for temporal correlation do not show a strong dependence on the mapping radius, mainly because $PM_{2.5}$ data are spatially averaged. For all cases and radii, the temporal correlation coefficients exceed 0.8, reflecting that the Station-Converted $PM_{2.5}$ data have a good performance in terms of temporal variation. However, Cases 2,3, 7 and 8 still outperform the other cases ($R > 0.9$ for all radii). Evaluation on temporal bias gives a similar result to the evaluation on spatial bias (see below) and is thus not shown.

For evaluation of spatial bias and correlation (Fig. 6a, and c), data at each $PM_{2.5}$ measurement site were averaged over the four months. The biases of Cases 1, 4 and 5 are very sensitive to the mapping radius, and the lowest biases are obtained for a radius of 0.5°–0.6°. These three cases also result in relatively low spatial correlation coefficients (<0.6). Cases 1 and 5 have similar results. Case 2 (with Cressman interpolation) leads to a relative high bias, except when the mapping radius exceeds 0.7°. Case 3 is derived from the IDW method, and thus its evaluation results do not vary with the mapping radius. Case 3 has a relatively low spatial correlation ($R = 0.60$) and a high bias (13.6 µg/m^3). Case 6 leads to the smallest mean bias, and its respective correlation coefficient is among the highest and does not change significantly with radius. Case 7 has the second highest spatial correlation coefficient (after Case 8) and a relatively small bias (within 10 µg/m^3 when radius is greater than 0.2°). This low bias suggests that using GEOS-Chem simulation results to adjust the spatial distribution of visibility inferred $PM_{2.5}$ helps to reduce the bias, a desirable outcome. Case 8 leads to the highest correlation coefficient, but it also has the greatest bias (>30 µg/m^3 for all mapping radius).

Fig. 6d further shows the RMA regression slope for the spatial variability of temporally averaged Grid-Converted $PM_{2.5}$ data. The slope of Case 8 is the highest and has small dependence on radius (i.e., between 1.35 and 1.40). The slopes of Case 1, 4 and 5 decline significantly with the increasing radius. Although Case 6 has the smallest mean bias and a high correlation coefficient, the regression slope of Case 6 is relatively low (<0.75) for all radii. The slope of Case 7 declines slightly with the increasing radius, and it remains between 0.85 and 1.05 for all radii.

Overall, Case 7 with a mapping radius of 0.3° has the most desired performance in both the temporal and the spatial domains. In particular, it has a relatively small mean bias (7.9 µg/m^3, or 9.4%), high correlation coefficients (0.80 spatially and 0.96 temporally) and better slope (1.0 spatially). A radius of 0.3° also helps preserve the high-resolution spatial information embedded in the visibility data and GEOS-Chem simulations. In the next section, we analyze the gridded results from this method in detail.

3.3. Spatio-temporal distribution of Grid-Converted $PM_{2.5}$ based on the selected station-to-grid conversion method (case 7)

Fig. 3e shows the gridded distribution of $PM_{2.5}$ concentrations averaged over the four months in 2014 based on Case 7 with a mapping radius of 0.3°. The spatial distribution is consistent with the observed one, such as the highest $PM_{2.5}$ concentrations over southern Hebei and the lowest over the northern regions. The gridded dataset corrects the underestimate in the model results and reduces the excessively high values in the Station-Converted data.

The scatter plots in Fig. 4c further evaluate the spatial distribution of Grid-Converted (Case 7) data against $PM_{2.5}$ observations. Gridded data were sampled from the grid cells covering the $PM_{2.5}$ measurement stations and on days with available $PM_{2.5}$ measurements. The correlation

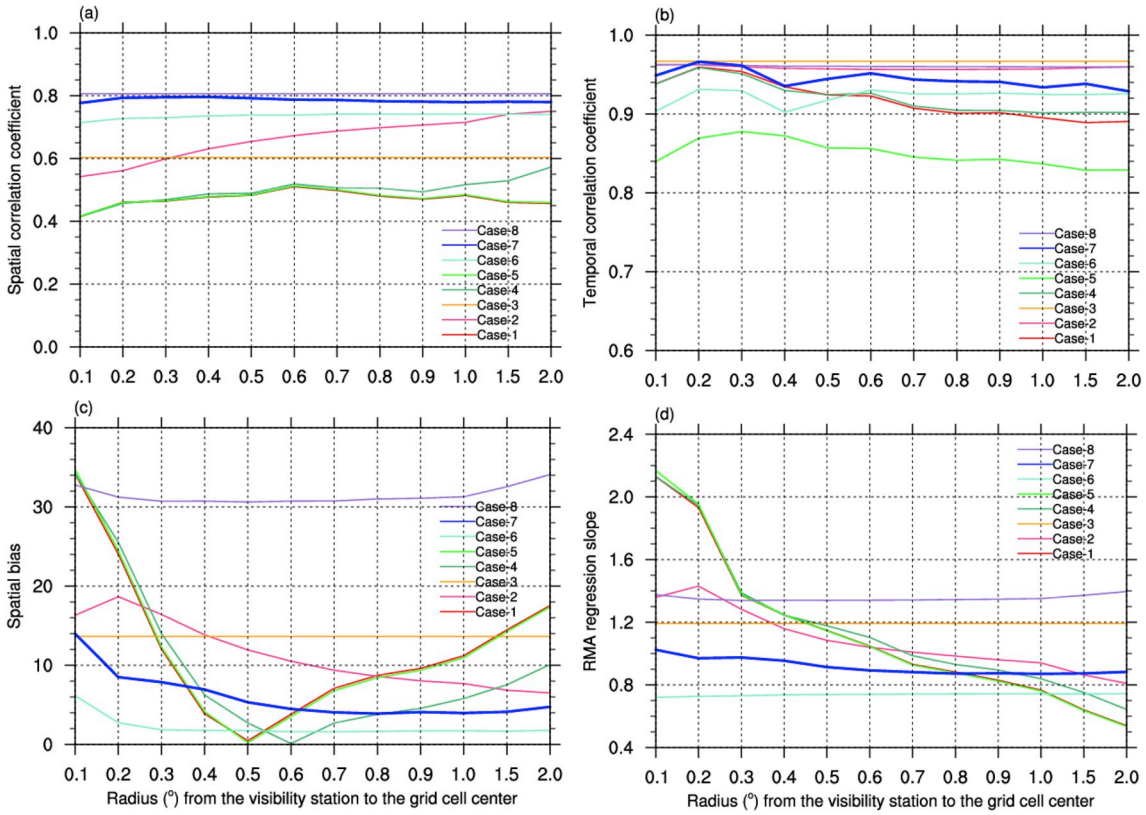

Fig. 6. (a) Spatial correlation, (b) temporal correlation, (c) spatial bias (units: $\mu g/m^3$) and (d) linear regression slope (for spatial data) of Grid-Converted $PM_{2.5}$ concentrations with respect to $PM_{2.5}$ measurements in each station-to-grid conversion case, as a function of the distance (i.e., radius ranging from 0.1° to 2.0°) from the visibility station to the grid cell center.

coefficient (R = 0.80) with the observed $PM_{2.5}$ are higher than model simulations (R = 0.73) and Station-Converted $PM_{2.5}$ (R = 0.49) alone. The mean bias (7.9 $\mu g/m^3$, or 9.4%), the RMA regression slope (1.0), and the small RMSE (17.6 $\mu g/m^3$) are also desirable, compared to the values for GEOS-Chem simulations (2.5 $\mu g/m^3$, 0.80, and 18.6 $\mu g/m^3$, respectively) and Station-Converted data (25.7 $\mu g/m^3$, 1.8, and 51.1 $\mu g/m^3$, respectively).

Fig. 5c shows the day-to-day variations of observed and Grid-Converted $PM_{2.5}$ concentrations (Case 7) in each month. For each day, data were selected from stations with available observations and converted values, and were further averaged over the NCP. Fig. 5c shows that Grid-Converted $PM_{2.5}$ data have a small bias of 9.4 $\mu g/m^3$ (or 11.4%); note that this value is slight different from the spatial bias (7.9 $\mu g/m^3$, or 9.4%) because of the difference between temporal and spatial sampling. The temporal variation of Grid-Converted $PM_{2.5}$ over the four months is consistent with the observed variation (R = 0.96, linear regression slope = 1.0), better than that of GEOS-Chem (R = 0.84, slope = 0.70) and Station-Converted (R = 0.96, slope = 1.3) $PM_{2.5}$. The Grid-Converted $PM_{2.5}$ data also capture the observed $PM_{2.5}$ peaks, which represent the pollution episodes, as well as the low values on clean days. They reproduce the seasonal variation of observed $PM_{2.5}$ mass concentrations, i.e., a higher mean value and day-to-day variability in winter and lower values in summer. The Grid-Converted $PM_{2.5}$ correct the temporally consistent overestimate in the Station-Converted $PM_{2.5}$ data and the wintertime underestimate and summertime overestimate in GEOS-Chem simulations.

4. Conclusions

This study offers a novel, plausible method to infer surface $PM_{2.5}$ mass concentrations on a 0.3125° longitude x 0.25° latitude grid, by combining the spatially dense high-frequency surface visibility measurements and GEOS-Chem simulations. Applying the method to the NCP in January, April, July and October 2014 shows good performance of the inferred data with respect to the official $PM_{2.5}$ measurements.

Specifically, after the visibility data are converted to $PM_{2.5}$ concentrations at each station and then each grid cell (based on Case 7 with a mapping radius of 0.3°), the derived gridded $PM_{2.5}$ data are both spatially and temporally consistent with the $PM_{2.5}$ measurements. The spatial and temporal mean biases are both within 10 $\mu g/m^3$. The temporal (day-to-day) correlation coefficient reaches 0.96 with a linear regression slope of 1.0. The spatial correlation coefficient reaches 0.80 with a regression slope of 1.0. The lower spatial correlation than the temporal correlation reflects that visibility data are spatially noisier (Lin and Li, 2016). Grid-Converted $PM_{2.5}$ improves upon GEOS-Chem simulations by correcting its wintertime underestimate and summertime overestimate. The temporal correlation coefficient, temporal regression slope, spatial correlation coefficient and spatial regression slope of converted $PM_{2.5}$ data are better than GEOS-Chem simulation results (0.84, 0.70, 0.73 and 0.80, respectively).

Future research will apply the inference method to all months in multiple years in the NCP to further test the robustness of the conversion method proposed here, with the goal of finally applying the method for a reliable retrieval of multi-decadal $PM_{2.5}$ variability embedded in the visibility data.

Declaration of competing interest

The authors declare that they have no known competing financial interests or personal relationships that could have appeared to influence the work reported in this paper.

Acknowledgments

This work was supported by the National Natural Science Foundation of China [grant numbers 41831175, 41775115, 41425019, and 41721004]. We acknowledge China Meteorology Administration (CMA) and China National Environmental Monitoring Center (CNEMC) for visibility and $PM_{2.5}$ data, respectively.

Appendix A. Supplementary data

Supplementary data to this article can be found online at https://doi.org/10.1016/j.atmosenv.2019.117121.

References

Allen, R.J., Norris, J.R., Kovilakam, M., 2014. Influence of anthropogenic aerosols and the Pacific Decadal Oscillation on tropical belt width. Nat. Geosci. 7, 270–274.
Boys, B.L., Martin, R.V., van Donkelaar, A., MacDonell, R.J., Hsu, N.C., Cooper, M.J., Yantosca, R.M., Lu, Z., Streets, D.G., Zhang, Q., Wang, S.W., 2014. Fifteen-year global time series of satellite-derived fine particulate matter. Environ. Sci. Technol. 48, 11109–11118.
Charlson, R.J., 1969. Visibility related to aerosol mass concentration - a review. ES T (Environ. Sci. Technol.) 3, 913–918.
Chen, J., Zhao, C., Ma, N., Liu, P., Gobel, T., Hallbauer, E., Deng, Z., Ran, L., Xu, W., Liang, Z., 2012. A parameterization of low visibilities for hazy days in the North China Plain. Atmos. Chem. Phys. 12, 4935–4950.
Craig, C.D., Faulkenberry, G.D., 1979. Application of ridit analysis to detect trends in visibility. Atmos. Environ. 13, 1617–1622.
Fairlie, T.D., Jacob, D.J., Dibb, J.E., Alexander, B., Avery, M.A., van Donkelaar, A., Zhang, L., 2010. Impact of mineral dust on nitrate, sulfate, and ozone in transpacific Asian pollution plumes. Atmos. Chem. Phys. 10, 3999–4012.
Fan, G., Ren, L., Mao, Y., 2017. Reconstruction of haze day database based on the comparison between manual and automatic observations. China Environ. Sci. 37, 1254–1261.
Fountoukis, C., Nenes, A., 2007. Isorropia II: a computationally efficient thermodynamic equilibrium model for K^+–$Ca2^+$–$Mg2^+$–$NH4^+$–Na^+–$SO4^{2-}$–NO^{3-}–cl^-–H_2O aerosols. Atmos. Chem. Phys. 7, 4639–4659.
Ge, B., Wang, Z., Lin, W., Xu, X., Li, J., Ji, D., Ma, Z., 2018. Air pollution over the North China Plain and its implication of regional transport: a new sight from the observed evidences. Environ. Pollut. 234, 29–38.
Geng, G., Zhang, Q., Martin, R.V., van Donkelaar, A., Huo, H., Che, H., Lin, J., He, K., 2015. Estimating long-term $PM_{2.5}$ concentrations in China using satellite-based aerosol optical depth and a chemical transport model. Remote Sens. Environ. 166, 262–270.
Geng, G., Zhang, Q., Martin, R.V., Lin, J.-T., Huo, H., Zheng, B., Wang, S., He, K., 2017. Impact of spatial proxies on the representation of bottom-up emission inventories: a satellite-based analysis. Atmos. Chem. Phys. 17, 4131–4145.
Giglio, L., Randerson, J.T., van der Werf, G.R., 2013. Analysis of daily, monthly, and annual burned area using the fourth-generation global fire emissions database (GFED4). J. Geophys. Res Biogeosciences. 118 (Issue 1), 317–328.
Guenther, A.B., Jiang, X., Heald, C.L., Sakulyanontvittaya, T., Duhl, T., Emmons, L.K., Wang, X., 2012. The Model of Emissions of Gases and Aerosols from Nature version 2.1 (MEGAN2.1): an extended and updated framework for modeling biogenic emissions. Geosci. Model Dev. (GMD) 5, 1471–1492.
Hudman, R.C., Moore, N.E., Martin, R.V., Russell, A.R., Mebust, A.K., Valin, L.C., Cohen, R.C., 2012. A mechanistic model of global soil nitric oxide emissions: implementation and space based-constraints. Atmos. Chem. Phys. 12, 7779–7795.
Husar, R.B., Husar, J.D., Martin, L., 2000. Distribution of continental surface aerosol extinction based on visual range data. Atmos. Environ. 34, 5067–5078.
Jaegle, L., Quinn, P.K., Bates, T.S., Alexander, B., Lin, J.-T., 2011. Global distribution of sea salt aerosols: new constraints from in situ and remote sensing observations. Atmos. Chem. Phys. 11, 3137–3157.
Lelieveld, J., Evans, J.S., Fnais, M., Giannadaki, D., Pozzer, A., 2015. The contribution of outdoor air pollution sources to premature mortality on a global scale. Nature 525, 367–371.
Li, Hao, Sun, X., 2009. Theoretical analysis on measurement error of forward scattering visibility meter. Infrared Laser Eng. 38, 1094–1098.
Li, J., Li, C., Zhao, C., Su, T., 2016. Changes in surface aerosol extinction trends over China during 1980-2013 inferred from quality-controlled visibility data. Geophys. Res. Lett. 43, 8713–8719.
Li, T., Shen, H., Yuan, Q., Zhang, X., Zhang, L., 2017. Estimating groundlevel PM2.5 by fusing satellite and station observations: a geo-intelligent deep learning approach. Geophys. Res. Lett. 44, 11985–11993.
Lim, S.S., Vos, T., Flaxman, A.D., 2012. A comparative risk assessment of burden of disease and injury attributable to 67 risk factors and risk factor clusters in 21 regions, 1990-2010: a systematic analysis for the global burden of disease study 2010. Lancet 381, 1276, 1276.
Lin, J.-T., Liu, Z., Zhang, Q., Liu, H., Mao, J., Zhuang, G., 2012. Modeling uncertainties for tropospheric nitrogen dioxide columns affecting satellite-based inverse modeling of nitrogen oxides emissions. Atmos. Chem. Phys. 12, 12255–12275.
Lin, J., McElroy, M.B., 2010. Impacts of boundary layer mixing on pollutant vertical profiles in the lower troposphere: implications to satellite remote sensing. Atmos. Environ. 44, 1726–1739.
Lin, J., Li, J., 2016. Spatio-temporal variability of aerosols over East China inferred by merged visibility-GEOS-Chem aerosol optical depth. Atmos. Environ. 132, 111–122.
Lin, J., Tong, D., Davis, S., Ni, R., Tan, X., Pan, D., Zhao, H., Lu, Z., Streets, D., Feng, T., Zhang, Q., Yan, Y., Hu, Y., Li, J., Liu, Z., Jiang, X., Geng, G., He, K., Huang, Y., Guan, D., 2016. Global climate forcing of aerosols embodied in international trade. Nat. Geosci. 9, 790–794.
Lin, J., van Donkelaar, A., Xin, J., Che, H., Wang, Y., 2014. Clear-sky aerosol optical depth over East China estimated from visibility measurements and chemical transport modeling. Atmos. Environ. 95, 258–267.
Liu, M., Bi, J., Ma, Z., 2017a. Visibility-based $PM_{2.5}$ concentrations in China: 1957-1964 and 1973-2014. Environ. Sci. Technol. 51 (22), 13161–13169.
Liu, M., Lin, J., Wang, Y., Sun, Y., Zheng, B., Shao, J., Chen, L., Zheng, Y., Chen, J., Fu, T.-M., Yan, Y., Zhang, Q., Wu, Z., 2018. Spatiotemporal variability of NO_2 and $PM_{2.5}$ over Eastern China: observational and model analyses with a novel statistical method. Atmos. Chem. Phys. 18, 12933–12952.
Liu, X., Liu, H., Hong, Z., Qin, Y., 2017b. Comparative analysis of visibility data between automatic and manual observation. J. Guizhou. Meteorol. 41 (6), 72–75.
Ma, Z., Hu, X., Huang, L., Bi, J., Liu, Y., 2014. Estimating ground-level $PM_{2.5}$ in China using satellite remote sensing. Environ. Sci. Technol. 48, 7436–7444.
Ni, R.-J., Lin, J.-T., Yan, Y.-Y., Lin, W., 2018. Foreign and domestic contributions to springtime ozone over China. Atmos. Chem. Phys. 18, 11447–11469.
Pye, H.O.T., Seinfeld, J.H., 2010. A global perspective on aerosol from low-volatility organic compounds. Atmos. Chem. Phys. 10, 4377–4401.
Rienecker, M.M., Suarez, M.J., Todling, R., Bacmeister, J., Takacs, L., Liu, H.-C., Gu, W., Sienkiewicz, M., Koster, R.D., Gelaro, R., Stajner, I., Nielsen, E., 2008. The GEOS-5 Data Assimilation Systeme Documentation of Versions 5.0.1, 9.1.0, and 5.2.0. NASA.
Shen, Z.X., Cao, J.J., Zhang, L.M., Zhang, Q., Huang, R.J., Liu, S.X., Zhao, Z.Z., Zhu, C.S., Lei, Y.L., Xu, H.M., Zheng, C.L., 2016. Retrieving historical ambient $PM_{2.5}$ concentrations using existing visibility measurements in Xi'an, Northwest China. Atmos. Environ. 126, 15–20.
Sinclair, D., Countess, R.J., Hoopes, G.S., 1974. Effect of relative humidity on the size of atmospheric aerosol particles. Atmos. Environ. 8, 1111–1117, 1967.
Song, Y., Tang, X., Fang, C., Zhang, Y., Hu, M., Zeng, L., Li, C., Michael, B., 2003. Relationship between the visibility degradation and particle pollution in Beijing. Acta Sci. Circumstantiae 23, 468–471.
Tan, H., Chen, H., Wu, D., Deng, X., Deng, T., Li, F., Zhao, X., Bi, X., 2010. The performance evaluation and data correction of the forward scattering visibility sensor. J. Trop. Meteorol. 26 (6), 687–693.
van Donkelaar, A., Martin, R.V., Brauer, M., Kahn, R., Levy, R., Verduzco, C., Villeneuve, P.J., 2010. Global estimates of ambient fine particulate matter concentrations from satellite-based aerosol optical depth: development and application. Environ. Health Perspect. 118, 847–855.
van Donkelaar, A., Martin, R.V., Spurr, R.J., Burnett, R.T., 2015. High-resolution satellite-derived $PM_{2.5}$ from optimal estimation and geographically weighted regression over North America. Environ. Sci. Technol. 49, 10482–10491.
Wang, Y.H., Liu, Z.R., Zhang, J.K., Hu, B., Ji, D.S., Yu, Y.C., Wang, Y.S., 2015. Aerosol physicochemical properties and implications for visibility during an intense haze episode during winter in Beijing. Atmos. Chem. Phys. 15, 3205–3215.
Wang, Y.H., Hu, B., Ji, D.S., Liu, Z.R., Tang, G.Q., Xin, J.Y., Zhang, H.X., Song, T., Wang, L.L., Gao, W.K., Wang, X.K., Wang, Y.S., 2014. Ozone weekend effects in the Beijing–Tianjin–Hebei metropolitan area, China. Atmos. Chem. Phys. 14, 2419–2429.
Wei, J., Huang, W., Li, Z., Xue, W., Peng, Y., Sun, L., Cribb, M., 2019. Estimating 1-km-resolution PM2.5 concentrations across China using the space-time random forest approach. Remote Sens. Environ. 231, 111221.
Wu, H., Tang, X., Wang, Z., Wu, L., Lu, M., Wei, L., Zhu, J., 2018. Probabilistic automatic outlier detection for surface air quality measurements from the China national environmental monitoring network. Adv. Atmos. Sci. 35, 1522–1532.
Xu, P., Tan, X., Cai, J., Liu, J., 2005. Study on influence factors of urban aerosol on visibility & extinction coefficient. Environ. Pollut Control. 27 (6), 410–413.
Zeng, S., Wang, G., 1999. Observation and instrument of visibility. Q. J. Appl. Meteorol. 10 (2), 207–212, 6.
Zhao, P.S., Zhang, X.L., Xu, X.F., Zhao, X.J., 2011. Long-term visibility trends and characteristics in the region of Beijing, Tianjin, and Hebei, China. Atmos. Res. 101, 711–718.
Zhang, L., Liu, L., Zhao, Y.H., Gong, S.L., Zhang, X.Y., Henze, D.K., Capps, S.L., Fu, Tzung-May, Zhang, Q., Wang, Y.X., 2015. Source attribution of particulate matter pollution over North China with the adjoint method. Environ. Res. Lett. 10, 084011.
Zhang, L., Kok, J.F., Henze, D.K., Li, Q., Zhao, C., 2013. Improving simulations of fine dust surface concentrations over the western United States by optimizing the particle size distribution. Geophys. Res. Lett. 40, 3270–3275.
Zhang, L., Liu, W., Hou, K., Lin, J., Song, C., Zhou, C., Huang, B., Tong, X., Wang, J., Rhine, W., Jiao, Y., Wang, Z., Ni, R., Liu, M., Zhang, L., Wang, Z., Wang, Y., Li, X., Li, S., Wang, Y., 2019. Air pollution exposure associates with increased risk of neonatal jaundice. Nat. Commun. 10, 3741.
Zhang, Q., Jiang, X., Tong, D., Davis, S.J., Zhao, H., Geng, G., Feng, T., Zheng, B., Lu, Z., Streets, D.G., Ni, R., Brauer, M., van Donkelaar, A., Martin, R.V., Huo, H., Liu, Z., Pan, D., Kan, H., Yan, Y., Lin, J., He, K., Guan, D., 2017. Transboundary health impacts of transported global air pollution and international trade. Nature 543 (7647), 705–709.

Zhang, Z., Xu, X., Qiao, L., Gong, D., Kim, S.J., Wang, Y., Mao, R., 2018. Numerical simulations of the effects of regional topography on haze pollution in Beijing article. Sci. Rep. 8, 5504.
Zheng, B., Tong, D., Li, M., Liu, F., Hong, C., Geng, G., Li, H., Li, X., Peng, L., Qi, J., Yan, L., Zhang, Y., Zhao, H., Zheng, Y., He, K., Zhang, Q., 2018. Trends in China's anthropogenic emissions since 2010 as the consequence of clean air actions. Atmos. Chem. Phys. Discuss. 1–27.
Zheng, Y., Zhang, Q., Liu, Y., Geng, G., He, K., 2016. Estimating ground-level $PM_{2.5}$ concentrations over three megalopolises in China using satellite-derived aerosol optical depth measurements. Atmos. Environ. 124, 232–242.